



Mapping the Thermal Condensation of Diffuse H I in the North Celestial Pole Loop

Mukesh Taank^{1,2} , Antoine Marchal² , Peter G. Martin² , and Luka Vujeva² ¹ Department of Mathematics and Statistics, University of Guelph, 50 Stone Road E., Guelph, ON N1G 2W1, Canada; mtaank@uoguelph.ca² Canadian Institute for Theoretical Astrophysics, University of Toronto, 60 St. George Street, Toronto, ON M5S 3H8, Canada

Received 2022 May 8; revised 2022 August 4; accepted 2022 August 19; published 2022 September 30

Abstract

The North Celestial Pole Loop (NCPL) provides a unique laboratory for studying the early stages of star formation, in particular the condensation of the neutral interstellar medium (ISM). Understanding the physical properties that control the evolution of its contents is key to uncovering the origin of the NCPL. Archival data from the NCPL region of the GHIGLS 21 cm line survey (9'4) are used to map its multiphase content with ROHSA, a Gaussian decomposition tool that includes spatial regularization. Column density and mass fraction maps of each phase were extracted along with their uncertainties. Archival data from the DHIGLS 21 cm (1') survey are used to further probe the multiphase content of the NCPL. We have identified four spatially (and dynamically) coherent components in the NCPL, one of which is a remarkably well-defined arch moving at about 14 km s^{-1} away from us that could be a relic of the large-scale organized dynamical process at the origin of the phase transition. The cold and lukewarm phases together dominate the mass content of the neutral gas along the loop. Using absorption measurements, we find that the cold phase exhibits slightly supersonic turbulence.

Unified Astronomy Thesaurus concepts: [Interstellar phases \(850\)](#); [Interstellar medium \(847\)](#); [Cold neutral medium \(266\)](#); [H I line emission \(690\)](#)

1. Introduction

The possible coexistence of two thermal phases in pressure equilibrium in the neutral atomic interstellar medium was described by Field (1965) and Field et al. (1969), but being an equilibrium theory, the amount of gas in each phase is indeterminate. It is expected that the condensation process from the warm neutral medium (WNM) requires perturbation by a dynamical event (e.g., colliding flows, expanding shells, turbulence) to trigger thermal instability, resulting in cooler and denser gas, the cold neutral medium (CNM). Indeed that is borne out by simulations (Hennebelle & Péroult 1999; Seifried et al. 2011; Saury et al. 2014; Bellomi et al. 2020), but the fractional amount of CNM arising is dependent on the details (Marchal & Miville-Deschênes 2021; Marchal et al. 2021). This condensation can be an evolutionary precursor to molecular gas (Rybarczyk et al. 2022) and star formation and so is of great interest and important in the interstellar medium (ISM).

The North Celestial Pole Loop (NCPL, Heiles 1984, 1989; Meyerdierks et al. 1991) provides a favorable environment in which to study the phase transition and its outcome empirically: finding gas and dust in a prominent feature so far from the Galactic midplane argues for a large-scale organized dynamical process (Marchal & Martin 2022), and being at intermediate latitude, the line of sight is not heavily contaminated by foreground and background emission.

Early observational evidence for multiphase gas in the NCPL was reported by Heiles (1989) in his study of the Zeeman effect for the 21 cm line. Although a one-Gaussian simultaneous fit to the Stokes parameter I and V spectra produced a fairly good solution, he found that a two-Gaussian model was needed to reproduce broad tails seen in the spectra. One component is

narrow like CNM, while the other is broader, reminiscent of the WNM. However, he also found that the broad component was typically narrower than expected for warm gas at 8000 K and concluded that the “WNM is not *all* at the same temperature” and that this might be the signature of gas in the thermally unstable regime. Focusing on Spider region at the “top” of the loop (in Galactic coordinates, see Figure 2), Blagrove et al. (2017, hereafter B17) found evidence that the intricate structures seen in H I (and in thermal dust emission) arise from the CNM phase.

In this paper, we use high-resolution H I data and the advanced multiphase analysis tool ROHSA (Marchal et al. 2019, hereafter M19) to quantify the multiphase properties of H I gas in the NCPL, thus probing the impact of the inferred dynamical process on the structure of the diffuse gas and providing additional clues about the dynamics. The long-standing question of the origin of the loop itself is taken up separately (Marchal & Martin 2022). Together, these works should motivate and constrain future simulations.

The paper is organized as follows. In Section 2 we present the H I data used in this work. Section 3 describes the Gaussian decomposition performed to model the H I spectra, and Section 4 provides a quantification of the thermal phases identified in the NCPL. Further evidence for cold gas from absorption lines is presented in Section 5. Finally, a discussion and summary are provided in Sections 6 and 7, respectively.

2. Data

We used the GHIGLS³ spectra of the H I 21 cm line brightness temperature, T_b , from the Green Bank Telescope (GBT; Martin et al. 2015), to probe the structure of neutral gas in the NCPL. Key characteristics of the relevant data cubes are as follows (Boothroyd et al. 2011): spatial resolution and pixel size 9'4 and 3'5, respectively; velocity resolution and channel



Original content from this work may be used under the terms of the [Creative Commons Attribution 4.0 licence](#). Any further distribution of this work must maintain attribution to the author(s) and the title of the work, journal citation and DOI.

³ GBT H I Intermediate Galactic Latitude Survey: <https://www.cita.utoronto.ca/GHIGLS/>.

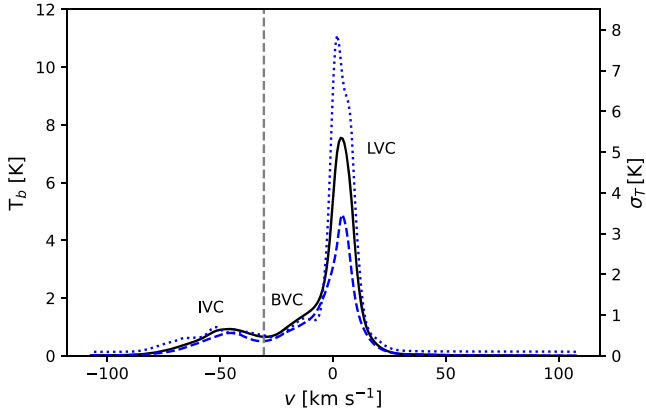


Figure 1. Mean H I spectrum of the region within the GHIGLS NCPL mosaic analyzed (the white box in Figure 2), showing relative positions of the IVC, BVC, and LVC. The black and dashed blue lines are the mean and median spectra, respectively (left y-axis). The dotted blue line is the standard deviation spectrum (right y-axis). Our analysis focuses on velocity channels to the right of the dashed gray line.

spacing 1.0 km s^{-1} and 0.8 km s^{-1} , respectively; velocities with respect to the local standard of rest (LSR) in a range at least $-310 < v < +210 \text{ km s}^{-1}$.

Figure 1 shows the mean, median, and standard deviation spectra of the region within the NCPL mosaic that we analyzed (the white square in Figure 2). It shows a strong peak of emission near 0 km s^{-1} (hereafter, low velocity component, or LVC) in which the loop is the most prominent. The secondary broader peak near -50 km s^{-1} is from what is referred to as the intermediate velocity component (IVC) gas. There is also significant emission bridging velocities in between, which does not show the loop and has some characteristics of IVC, but will be distinguished as a bridge velocity component (BVC) in the analysis. In the full NCPL mosaic, there is weak emission in the high-velocity range, belonging to the high-velocity cloud (HVC) complexes A and C (Planck Collaboration XXIV 2011), but there is none in the region that we analyzed. Note that the standard deviation spectrum and mean spectrum have higher contrast relative to each other and to the median spectrum in the LVC compared with BVC and IVC. As we shall see, this is due to the small-scale structure in the cold gas that dominates in the LVC.

In this work, we analyze the spectral range of $-30.56 < v < 53.17 \text{ km s}^{-1}$, which includes adequate emission-free channels on the positive side, and the BVC on the left.⁴ We specifically want to model the LVC gas; to do that accurately, we must include the BVC, because its spectral components could overlap with the LVC. On the other hand, the IVC is sufficiently weak and separated from the LVC in this region that it can be ignored. See also Figure 7 in Section 4.3 for validation of this approach.

The H I spectra in the NCPL are complex, a blend of these different components within which line widths from various thermal phases also differ. This will be discussed in Section 4. Spectra are also quite variable spatially. Figure 2 shows the total column density map of the GHIGLS NCPL mosaic (inside the black contour) as integrated over the selected velocity range of interest. For completeness, EBHIS data (Kerp et al. 2011; Winkel et al. 2016) in the velocity range $-29.52 < v < 51.63 \text{ km s}^{-1}$

⁴ Specifically, counting from channel 0 in the original cube, this is the 105 channel range starting at channel 200.

were added to cover all latitudes and longitudes shown in Figure 2.⁵

In this paper, we analyzed a 15° square region centered near Galactic coordinates $(132^\circ, +38^\circ)$,⁶ shown as the white square in Figure 2. This region, which we still refer to as the NCPL, captures the main loop while avoiding some of the extra-Galactic emission from the M81/M82 group on the western edge. For the analysis below, pixels contaminated by extra-Galactic emission (some even masked in GHIGLS because of corrupted baselines) were in-painted as described in Appendix A.

3. Spectral Decomposition

3.1. Model

We performed a spectral decomposition of NCPL using the publicly available Gaussian decomposition code, ROHSA⁷ M19, that was designed to facilitate phase separation using 21 cm data. The algorithm implemented in ROHSA is based on a regularized nonlinear least-square criterion that takes into account the spatial coherence of the emission and the multiphase nature of the gas.

The model $\tilde{T}_b(v, \theta(\mathbf{r}))$ used to fit the measured brightness temperature $T_b(v, \mathbf{r})$ at a projected velocity v and coordinates \mathbf{r} is given by:

$$\tilde{T}_b(v, \theta(\mathbf{r})) = \sum_{n=1}^N G(v, \theta_n(\mathbf{r})), \quad (1)$$

where each of the N Gaussians are parameterized by three 2D spatial fields $\theta_n(\mathbf{r}) = (\mathbf{a}_n(\mathbf{r}), \mu_n(\mathbf{r}), \sigma_n(\mathbf{r}))$: amplitude $\mathbf{a}_n \geq 0$, mean velocity μ_n , and standard deviation σ_n .

3.2. Optimization of the Gaussian Parameters

The parameters $\hat{\theta}$ are obtained by minimizing the cost function described in Equation (8) of M19, the cost function being a regularized nonlinear least-square criterion containing several distinct “energy” terms. The first term of this cost function is

$$\frac{1}{2} \|L(v, \theta)\|_S^2 \equiv \frac{1}{2} \chi^2(\theta) \quad (2)$$

where $L(v, \theta(\mathbf{r}))$ is the residual between the model and the data, which is to be compared to the noise S , as in the familiar χ^2 . To describe the noise properties, we adopted the 3D prescription discussed by Boothroyd et al. (2011):

$$S(v, \mathbf{r}) = S_e(\mathbf{r})(1 + T_b(\mathbf{r})/T_{\text{sys}}), \quad (3)$$

where the 2D map of the standard deviation of the noise $S_e(\mathbf{r})$ is calculated from emission-free end channels (in the case of GHIGLS, supplied with the archival data), and T_{sys} is the system temperature, typically 20 K for the GBT L -band observations. The original ROHSA code was augmented to work with 3D noise, rather than the standard 2D noise.

⁵ Surveyed with the Effelsberg 100 meter radio telescope, EBHIS has a spatial resolution comparable to GHIGLS ($10''.8$ and $9''.4$ beams, respectively).

⁶ Specifically, counting pixels from (0,0) at the lower left of the full NCPL mosaic, this is the 256-pixel square, with the lower left corner at coordinate (295, 154).

⁷ <https://github.com/antoinemarchal/ROHSA>

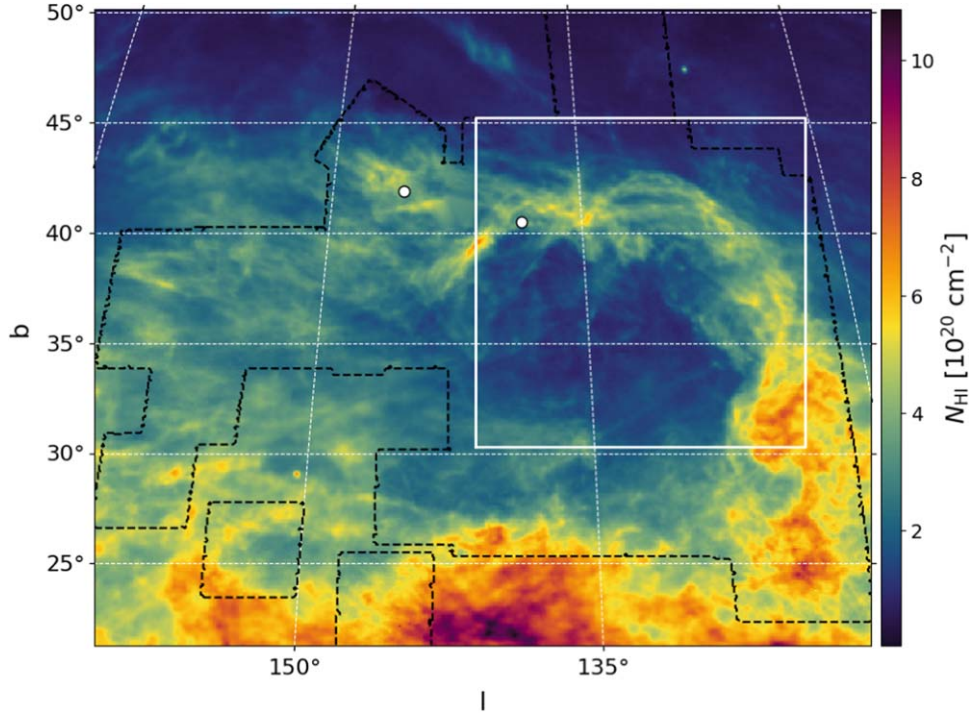


Figure 2. In-painted column density map of the GHIGLS NCPL mosaic integrated over the spectral range $-30.56 < v < 53.17 \text{ km s}^{-1}$, calculated in the optically thin regime. Outside the black dashed contour are shown data from EBHIS over a similar velocity range ($-29.52 < v < 51.63 \text{ km s}^{-1}$). The solid white square shows the 256×256 pixel region on which our analysis is focused. White points represent the positions of the Ursa Major (UM; left) and DRAO Deep Field (DF; right) absorption sources from the DHIGLS survey.

In addition, the cost function includes four terms that regularize certain 2D parameter maps of the model. For the first three, a Laplacian filtering is applied on each of the three Gaussian parameter maps ($a_n(r)$, $\mu_n(r)$, $\sigma_n(r)$) to penalize deviations at high spatial frequencies and ensure a spatially coherent encoding of the signal. The magnitudes of these terms are controlled by the hyper-parameters (λ_a , λ_μ , λ_σ).

To ensure a solution in which phases are identifiable according to distinct velocity dispersions (phase separation), M19 introduced a further term in the cost function, $\frac{1}{2} \|\sigma_n - m_n\|_2^2$, where m_n is an unknown scalar value to be estimated and $\lambda_{\sigma'}$ is the corresponding hyper-parameter, again chosen by the user. This is a global penalty on the variance of each σ_n map, minimizing the variance of σ_n across the field. The magnitude of m_n found enables an association with a thermal phase of the neutral ISM (i.e., WNM, LNM, or CNM, for large through small values, respectively).

In this original implementation, the absolute difference of $\sigma_n - m_n$ is higher for a broad Gaussian than for a narrow Gaussian, which results in a stronger penalty in the cost function and a narrowing of the distribution of σ_n for Gaussians associated with the WNM (see, e.g., Figures 16 and 19 in M19). To avoid this effect, we use a normalized version,

$$V(\theta, m) = \frac{1}{2} \lambda_{\sigma''} \sum_{n=1}^N \left\| \frac{\sigma_n - m_n}{m_n} \right\|_2^2, \quad (4)$$

that penalizes the relative difference between σ_n and m_n . We denote the hyper-parameter as $\lambda_{\sigma''}$, rather than $\lambda_{\sigma'}$ as seen in M19, to signal that this normalized version is being used.

In ROHSA, starting values of parameters at full resolution are obtained through a multi-resolution process beginning with a fit of the average spectrum of the entire field (M19). This procedure aims to facilitate the regularization and to accelerate the search for the initial parameters. The parameters of the Gaussians required to fit this mean spectrum are obtained by a bespoke procedure within ROHSA (M19). For later assessment in Section 4.2, we altered ROHSA to be able to optimize the fit of the mean spectrum given starting guesses for the parameters, or to simply specify the initial parameters at this top level.

3.3. Choosing the User Parameters

Application of ROHSA requires choosing values for the number of Gaussians and the four hyper-parameters of the model. These choices need to be revisited for each specific data set (e.g., Marchal et al. 2021). To enable a more efficient exploration of these free parameters, we specified that (λ_a , λ_μ , λ_σ), which control similar terms in the cost function, be the same. The decomposition presented in this work was obtained using ($N = 11$, $\lambda_a = \lambda_\mu = \lambda_\sigma = 100$, and $\lambda_{\sigma''} = 100$).

The choice of the number of Gaussians N is driven by our desire to fully describe the signal while ensuring that the regularization terms in the cost function have the magnitude required to enable a spatially coherent solution and a multi-phase separation. Given the complexity of the signal coupled with the fact that we ought to describe the LVC and BVCs simultaneously, we explored the parameter space $N = [8 - 15]$ and made use of the mean contribution to chi-square,

$$\langle \chi^2 \rangle = \sum_r \left(\frac{L(v, \theta(r))}{S(v, r)} \right)^2 / 256^2, \quad (5)$$

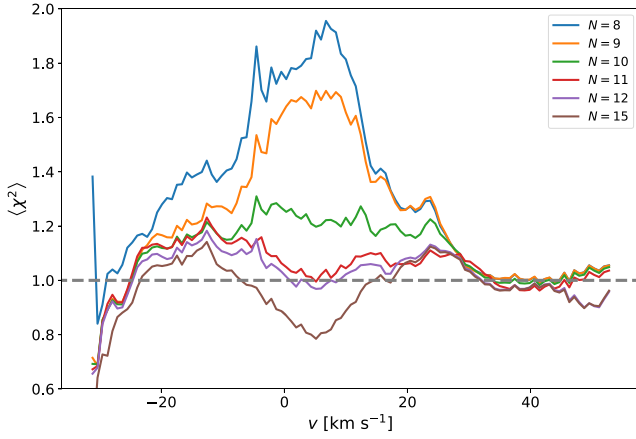


Figure 3. Spectrum of mean contribution to chi-square for Gaussian models fit with different number of Gaussians. Horizontal line indicates $\langle \chi^2 \rangle = 1$.

to find the optimal value. Note, 256^2 is the total number of pixels in our region of focus.

Figure 3 shows the mean contribution to chi-square as function of velocity for increasing values of N . The horizontal gray dashed line indicates $\langle \chi^2 \rangle = 1$, the expected value for a model close to the data. As a selection criterion, we chose to keep the model closest to the horizontal line (in the LVC range of interest), $N = 11$, without going below it, indicating that the data start to be over-fitted by the model.

The set of three hyper-parameters controlling the smoothness of the parameter maps was chosen empirically to correlate adjacent pixels on a spatial scale close to the beam of the instrument. In experimenting with this set of parameters, the optimal model was found to have $\lambda_a = \lambda_\mu = \lambda_\sigma = 100$. A lower value shows pixelated parameter maps, while a higher value alters the native resolution of the observation and prevents the model from being close to the data. Finally, we chose $\lambda''_\sigma = 100$ to ensure the phase separation, while not imposing too much penalty on the total cost function.

This specific choice of hyper-parameters does not guarantee that appropriate Gaussians will be found to fit every detail in the cube, due primarily to its complexity. However, in such circumstances it might not matter to the overall goals of the decomposition, even if such a failure is detectable (e.g., in the BVC range), comparing the model with the data.

3.3.1. Map of χ^2

Although χ^2 is not the full cost function minimized by ROHSA, we expect that values for a good fit would be distributed like χ^2 for the appropriate number of degrees of freedom. We used a reduced and spatially resolved version of Equation (2),

$$\chi_r^2(\theta(\mathbf{r})) = \sum_v \left(\frac{L(v, \theta(\mathbf{r}))}{S(v, \mathbf{r})} \right)^2 / k \quad (6)$$

where $k = 150 - 3N_{\text{eff}}$ is the number of degrees of freedom, with 150 the number of velocity channels and N_{eff} the number of Gaussians contributing to the fit. In practice, $N_{\text{eff}} < N$ in any pixel because the regularization limits the use of all Gaussians available, especially the term penalizing the variance of each σ_n map. Although a precise map of N_{eff} cannot be predicted, it is possible to approximate it a posteriori by counting locally the

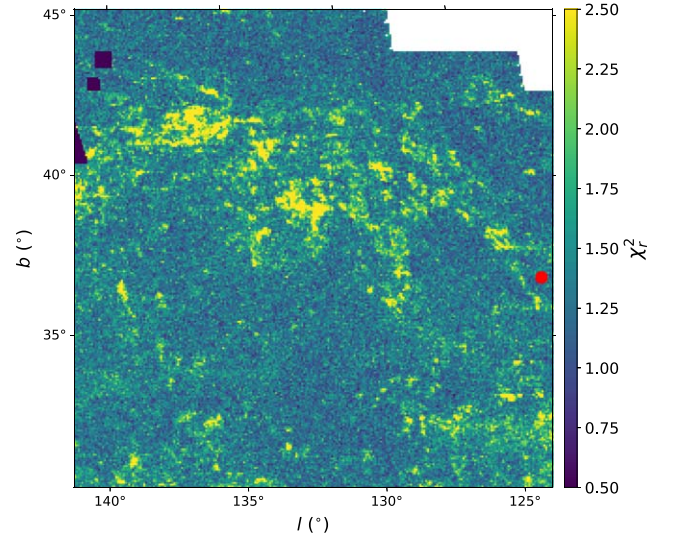


Figure 4. Map of the reduced χ^2 obtained with ROHSA on the NCPL. The location of the spectral decomposition shown in Figure 6 is annotated by the red point.

number of Gaussians that contribute significantly to the total column density, say at least 1%.

Figure 4 shows the map of χ_r^2 . The dark regions in the upper left are pixels that have been in-painted to avoid modeling extra-Galactic emission from the M81/M82 group (see Appendix A). The map is relatively flat, which illustrates that the model fits the data reasonably well. The mean, median, and standard deviation are 1.43, 1.37, and 0.39, respectively. In areas where the loop and Spider shape are not seen, the χ_r^2 is very close to 1. We found that the areas where χ_r^2 is highest are due primarily to a poor fit in the BVC range.⁸ This does not affect significantly the goodness of fit in the LVC range where the NCPL is located.

3.4. A Representative Solution

3.4.1. The σ - μ Diagram

The corresponding Gaussian parameters for all spatial pixels are summarized in the 2D histogram of the column-density-weighted σ - μ parameters, seen in Figure 5. There are 11 clusters of points that correspond to the N Gaussians used by ROHSA to fit the data. In particular, the separation vertically into clusters of broader and narrower components results from the hyper-parameter λ''_σ . Black points show the column-density-weighted average of each cluster, which are summarized in Table 1. The velocity dispersions of all clusters range from about 1 to 8 km s^{-1} . This reveals the multiphase nature of the gas, both in the BVC and in the LVC range where the NCPL is located.

The corresponding Gaussian parameter maps, sorted by increasing mean velocity, are shown in Appendix B. Rather than present a map of the amplitudes a_n , we used the analytic integral of the Gaussians to evaluate the column density maps (proportional to $a_n \sigma_n$); these are presented in Figure B1. Maps of mean μ_n and dispersion σ_n are presented in Figures B2 and B3, respectively.

⁸ Visualization of the residual cube provided a good overview of any deficiencies in the fit, which are most present in the BVC range.

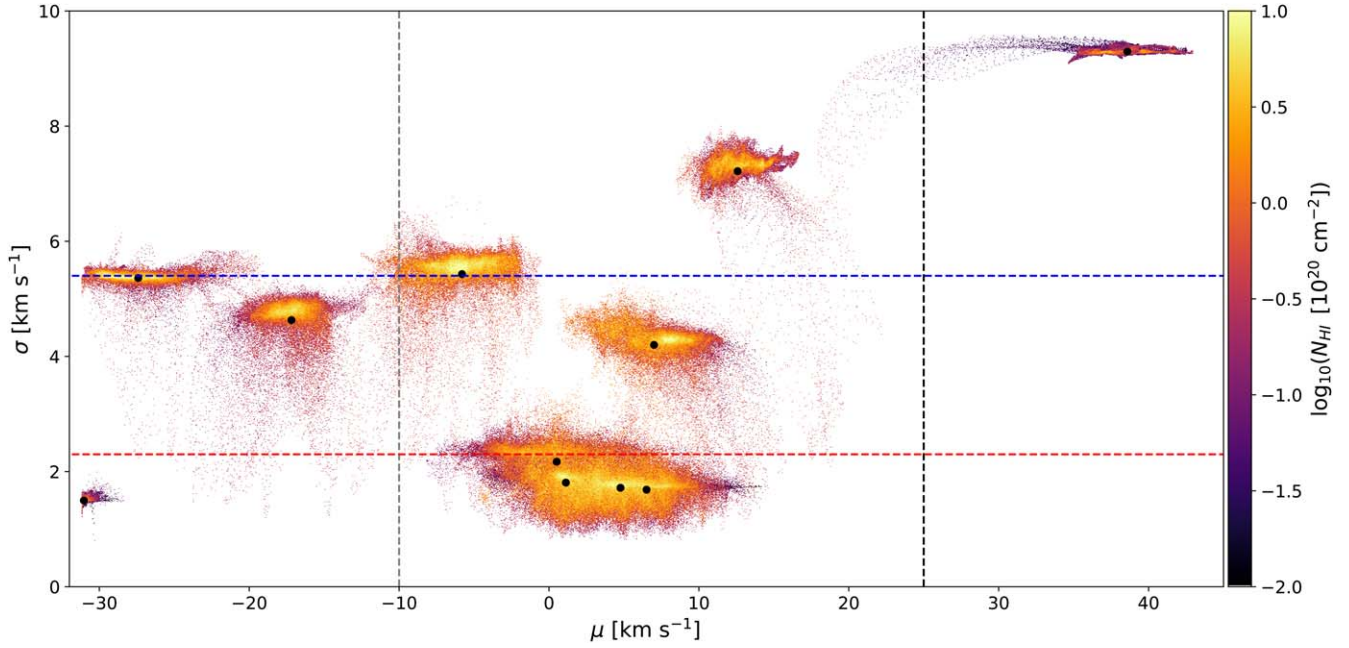


Figure 5. 2D probability distribution function of N_{HI} of the Gaussians in the σ - μ plane. Vertical gray line at $\mu = -10 \text{ km s}^{-1}$ shows the boundary separating the BVC and LVC. Vertical black line at $\mu = 25 \text{ km s}^{-1}$ represents the outer limit on the LVC range. Horizontal lines at $\sigma = 2.3 \text{ km s}^{-1}$ (red) and 5.4 km s^{-1} (blue) represent the CNM/LNM and LNM/WNM boundaries (see Section 4). Black points within the clusters represent the column-density-weighted means of each Gaussian cluster, tabulated in Table 1.

Table 1
Mean Kinematic Properties (in km s^{-1}) of Gaussians Inferred from the NCPL Data

	G_1	G_2	G_3	G_4	G_5	G_6	G_7	G_8	G_9	G_{10}	G_{11}
$\langle \mu_n \rangle$	-30.2	-26.6	-16.4	-5.0	1.3	1.9	5.6	7.3	7.8	13.4	39.4
$\langle \sigma_n \rangle$	1.5	5.4	4.6	5.4	2.2	1.8	1.7	1.7	4.2	7.3	9.3

3.4.2. LVC and BVC

Building on this, we refined our LVC/BVC classification based on the Gaussian parameter space. The column density map of each cluster in Figure 5 was visualized from Figure B1 to determine if it belongs to the loop. We found that Gaussians G_4 – G_{10} show a loop-like structure and can be classified as LVCs. Their column-density-weighted velocity centroids are included in the velocity range $-10 < v (\text{km s}^{-1}) < 25$ (see Table 1), denoted by the gray and black vertical dashed lines in Figure 5. Other Gaussians are classified as BVCs. As expected from our classification, the resulting total N_{HI} maps of the BVC and the LVC (not shown here) do not show any striking correlations.

Figure 6 shows an example spectrum (top) where 10 out of 11 Gaussians (i.e., G_1 – G_{10}) are used to fit the data. G_{11} is centered on $\mu = 40 \text{ km s}^{-1}$ and has low amplitude. This particular line of sight, whose location is annotated by the red point in Figure 4, is representative of both data and decompositions.⁹ The residual spectrum is shown in the bottom panel. Gaussians G_4 – G_{10} encoding the LVC range are, as Figure 5 shows, composed of narrow (red), intermediate (green), and wide (blue) components. This specific choice to color code will be discussed in Section 4.

⁹ We made use of an original visualization tool wherein we could hover over any pixel in the map and view the corresponding spectrum. We found Figure 6 to be typical of decompositions of the data.

4. Thermal Phases in the NCPL

4.1. Phase Separation

Focusing on the LVC, mapping out the different thermal phases requires clustering the Gaussian components based on their mean velocity dispersion and mean velocity in Figure 5, and on the morphology of their column density maps in Figure B1.

Gaussians G_5 – G_8 are narrow and together form a single large cluster in σ – μ space. Their column density maps display the loop prominently and are structured on small angular scales. We can readily identify the “legs” of the Spider. Outside of the loop, however, their column densities are comparatively low. Hereafter, this group of Gaussian clusters describing the cold gas will be simply called CNM. Gaussians G_4 and G_{10} are broad but have very distinct morphologies. While G_4 at $\langle \mu_4 \rangle = -5 \text{ km s}^{-1}$ shows diffuse emission over the entire field, including the low-density regions below and above the loop, G_{10} at $\langle \mu_{10} \rangle = 13.4 \text{ km s}^{-1}$ shows a striking continuous arch. The two warm components described by G_4 and G_{10} will be called more memorably WNM_D and WNM_A , respectively, adopting the standard abbreviation WNM for a warm neutral medium “phase,” with subscripts D (“diffuse”) and A (“arch”). They are kept separate based on their different morphologies and large velocity separation.

Finally, Gaussian G_9 has intermediate velocity dispersions, usually associated with lukewarm gas. This will be called

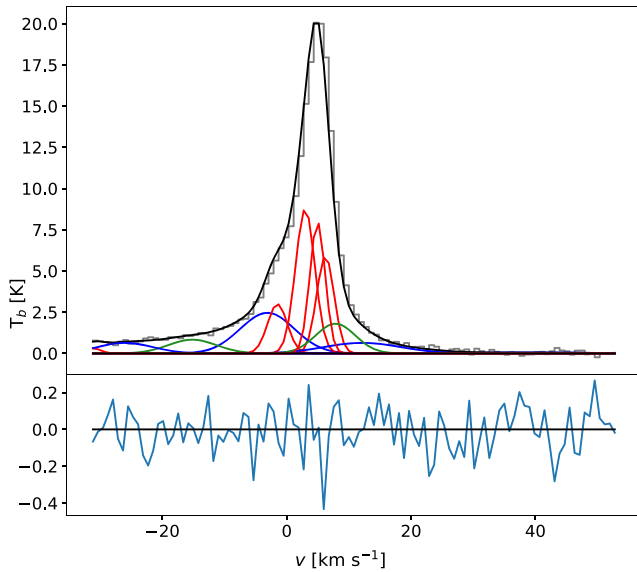


Figure 6. The upper panel is an example of the Gaussian decomposition obtained by ROHSA for the spectrum corresponding to the position annotated by the red point in Figure 4. Original signal is shown in gray and the total brightness temperature encoded by ROHSA is shown in black. Colored lines represent the individual Gaussian components. Red represents CNM, green represents LNM, and blue represents WNM. The lower panel shows the residual spectrum.

LNM. Note that its column density morphology is closer to those of the narrow Gaussians.

On this basis, for subsequent evaluation of the means and uncertainties of column densities, we define that the column-density-weighted velocity dispersions of CNM, LNM, and WNM Gaussian clusters satisfy $\langle \sigma_n \rangle < 2.3 \text{ km s}^{-1}$, $2.3 < \langle \sigma_n \rangle (\text{km s}^{-1}) < 5.4$, and $\langle \sigma_n \rangle > 5.4 \text{ km s}^{-1}$, respectively. These boundaries are annotated by the blue and red horizontal lines in Figure 5. These boundaries translate, for purely thermal broadening, into kinetic temperatures $T_k \sim 520 \text{ K}$ and $T_k \sim 3400 \text{ K}$. Gaussians shown in Figure 6 are color coded according to this separation (WNM: blue, LNM: green, and CNM: red). While this operational definition of CNM by grouping of clusters is natural in the context of Gaussian component separation for this specific field, it is neither uniquely definitive nor applicable to others. Note also that part of the broadening can be due to turbulence (Section 5.1.2), so that the CNM gas would be cooler than 520 K.

4.2. Stability Analysis and Evaluation of Uncertainties

4.2.1. Reevaluating N

It is useful at this point to reevaluate the number of Gaussians needed to describe the emission containing the NCPL. Ensuring that the data are not “over-fitted” allows us to avoid a possible leakage from the cold phase model to the warm phase model—broad Gaussians can always be described by a sum of narrow Gaussians. The seven Gaussians previously identified as belonging to the loop were combined to generate a model PPV position-position-velocity (PPV) cube of the LVC gas. Because this model is noise-free, we injected a 3D Gaussian random noise using the prescription presented in Equation (3) (see Section 3.2). We applied ROHSA on this model cube for $N = [5-8]$ to bracket the original number of Gaussians used to model the LVC gas ($N = 7$). The hyper-parameters were kept the same.

Similarly to Figure 3, we inspected the mean contribution to chi-square in the velocity range of interest. The decomposition of our model cube with five or six Gaussians prevents us from completely encoding the data. $N = 7$ remains closest to the expected value of $\langle \chi^2 \rangle = 1$. We retain this number as the optimal choice for describing the multiphase structure of H I gas in the NCPL.

4.2.2. Uncertainties

Although we have determined the optimal number of Gaussians needed to describe the NPCL data in the LVC range, it remains that their position in the parameter space can vary due to the nonlinear nature of the model. There are several possible combinations/arrangements of the seven Gaussians that can be used to obtain a solution that satisfies our quality criteria (see Section 3.3).

To explore the degeneracy of the solution, we have repeated the Gaussian decomposition of the model cube using three series of runs. The first two series, composed of 50 runs each, follow the methodology developed by Marchal et al. (2021, see their Section 4.1.1). The first series explores how the outcome of the decomposition is influenced by the injection of 50 different instance of the noise. The hyper-parameters were kept the same. The second series explores the impact of the hyper-parameters on the solution. It entails generating 50 runs using random perturbations of the four ROHSA hyper-parameters in a $\pm 10\%$ interval around the original values. Here, the injected 3D Gaussian random was kept the same.

The third series is original to this work. It explores the sensitivity to how ROHSA is initialized (i.e., choice of the initial parameters at the top level of the multi-resolution process, or descent; see Section 3.2). It entails generating 50 runs where the seven Gaussians needed to initialize the descent are randomly selected from the original σ - μ diagram shown in Figure 5. Specifically, we selected pixels within the following constraints: 5 km s^{-1} in μ and 1 km s^{-1} in σ relative to the column-density-weighted means of each Gaussian cluster. This ensures that these Gaussians provide a good average representation of the data. Here, the hyper-parameters were kept the same as the original run.

For each of the 50-run series, the outcomes were examined in σ - μ space, showing that the clusters observed in Figure 5 are quite stable, including the need for the intermediate LNM component.

For each run, we performed a phase separation by grouping the seven Gaussians into the four components CNM, LNM, WNM_D, and WNM_A based on the mean velocity dispersion limits established in Section 4.1. Then for each series, maps of the mean column density and its standard deviation were generated for the four components. Intercomparison of these results between series revealed that they were compatible.

Therefore, all 50 runs of each series were combined to calculate maps for two phase-separated quantities of interest discussed in the following section: column density and mass fraction, and their standard deviations. Finally, for each quantity the contributions from the three series were summed in quadrature to yield the total uncertainty (the contribution from the third series was generally slightly higher than from the first and second).

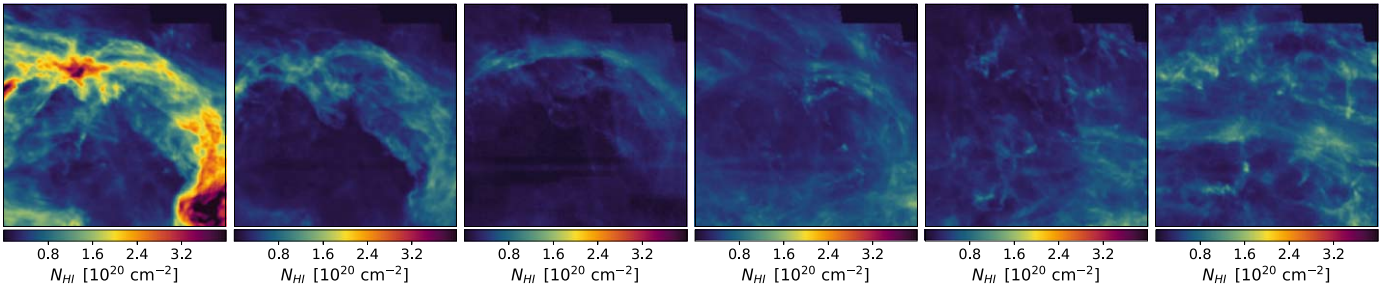


Figure 7. Column density maps of the thermal phases in the LVC, plus maps of the total BVC and IVC, in the NCPL. From left to right, the maps represent the CNM, LNM, WNM_A, WNM_D (all of the LVC), BVC, and IVC. Maps have the same dynamical range (color bar) to highlight the dominance of the CNM.

4.3. Column Density and Mass Fraction Maps

Figure 7 shows the N_{HI} maps in column one of Figure 8, as well as the N_{HI} maps of the BVC and IVC, but all with the same dynamical range (color bar) as in the CNM map. This shows just how abundant the cold gas in the LVC is, and further verifies the large mass fraction of the CNM compared with the other phases and velocity components.

Figure 8 shows column density and mass fraction maps (first and third column) with their associated standard deviation maps (second and fourth column) of the thermal phases in the NCPL. Rows from top to bottom show the CNM, LNM, WNM_A, and WNM_D, respectively. To facilitate the localization of the loop in the mass fraction maps, we overlaid contours of the total LVC column density using levels of 1×10^{20} (cyan) and $2 \times 10^{20} \text{ cm}^{-2}$ (yellow). Note that the main attributes of the Spider, like its body and “legs,” are all within the cyan and yellow contours. The average properties (column density and mass fraction) for each component are tabulated in Table 2, where we distinguished “on loop” and “off loop” using the $2 \times 10^{20} \text{ cm}^{-2}$ level shown by the yellow contour.

The CNM component (first row) displays the loop prominently. We can identify the bright body of the Spider as well as its individual “legs.” Others areas of highest column densities include Polaris, located in the southwest part of the field, and a body located at the eastern edge of the field, toward Ursa Major. The CNM mass fraction “on loop” and “off loop” are 0.50 ± 0.15 and 0.36 ± 0.12 , respectively. Locally, in the body of the Spider and the southern part of Polaris, the CNM mass fraction range up to about 0.72.

The LNM (second row) also shows the loop prominently but with a lower column density contrast. The body of the Spider is less pronounced and shows small-scale structure around it. We can identify the bright body toward Ursa Major in this map as well. As with the body of the Spider, Polaris appears less bright. The overall mass fraction in the LNM is lower than in the CNM with an average “on loop” and “off loop” of 0.21 ± 0.15 and 0.16 ± 0.14 , respectively. Note that standard deviation maps of LNM and CNM are highly correlated, highlighting the degeneracy of the solution. These numbers should be considered carefully and their combined mass fraction considered a more robust estimate of the amount of cold and lukewarm gas mixed together.

As presented previously, WNM_A shows a continuous arch. It coincides spatially with the top of the loop traced by the cold and lukewarm gas from the center of the field to the west. Toward the east, “legs” come out of the body of the Spider and no longer follow the warm arch. This can be visually appreciated in the WNM_A mass fraction map, where contours of the loop are displayed, and in the three-phase RGB view shown in Figure 9, where phases CNM, LNM, and WNM_A+WNM_D are color coded

by red, green, and blue, respectively. Mass fractions “on loop” and “off loop” are similar, with values of 0.11 ± 0.04 and 0.13 ± 0.04 , respectively.

WNM_D (fourth row) is much more diffuse on large scales but has bright features on small scales at various locations in the field that sometimes do not coincide with the loop. The fact that WNM_D overlaps with the BVC range, which shows similar structures at small scales, may be a clue that these clouds physically coincide with IVCs located farther along the line of sight but appear at lower velocities in projection. As for the CNM, mass fractions “on loop” and “off loop” are significantly offset, with values of 0.16 ± 0.08 and 0.32 ± 0.15 , respectively. In the southern part of the field, which coincides with the low total column density region of the NCPL (i.e., in the inner part of the loop), the mass fraction of warm gas ranges up to 0.61.

4.3.1. Dependence on Phase Separation Boundaries

We compared our boundaries for the LVC in the NCPL field with those found by Kalberla & Haud (2018) over the full sky from their Gaussian decompositions. In their Figure 5, the boundary between CNM and LNM is about 5.62 km s^{-1} FWHM ($\sigma = 2.39 \text{ km s}^{-1}$) and between LNM and WNM about 15.84 km s^{-1} FWHM ($\sigma = 6.73 \text{ km s}^{-1}$). These are (coincidentally) quite comparable to the boundaries $\sigma = 2.3 \text{ km s}^{-1}$ (CNM/LNM) and $\sigma = 5.4 \text{ km s}^{-1}$ (LNM/WNM) discussed above. The boundaries vary from field to field given their unique dynamical histories and we are confident in the particular choices we have made.

Looking at the LVC clusters with low σ in Figure 5, if we increased the red boundary anywhere up to 4 km s^{-1} , there would no difference in what we call CNM. On the other hand, if we lowered the blue boundary, cluster G_4 could become LNM. This would substantially increase the total LNM, adding gas at a distinctly different velocity.

Moving the LNM/WNM boundary as low as 4.5 km s^{-1} would make no difference, but if we increased it, then WNM_D would be reclassified as LNM. Given its very different morphology, we would call it LNM_D and not just add it to the other LNM cluster. However, the CNM would still dominate in terms of mass fraction. Indeed, having LNM dominate would seem very unusual.

Moving the boundaries would also impact the standard deviation maps in columns 2 and 4 of Figure 8. Most significantly, raising the CNM/LNM boundary would actually decrease our estimate of the uncertainty of the CNM and LNM column densities and their mass fractions, because there would be fewer Gaussians in the 150 runs where the slight change of the dispersion would be enough to have it cross the boundary and be reclassified as the other phase.

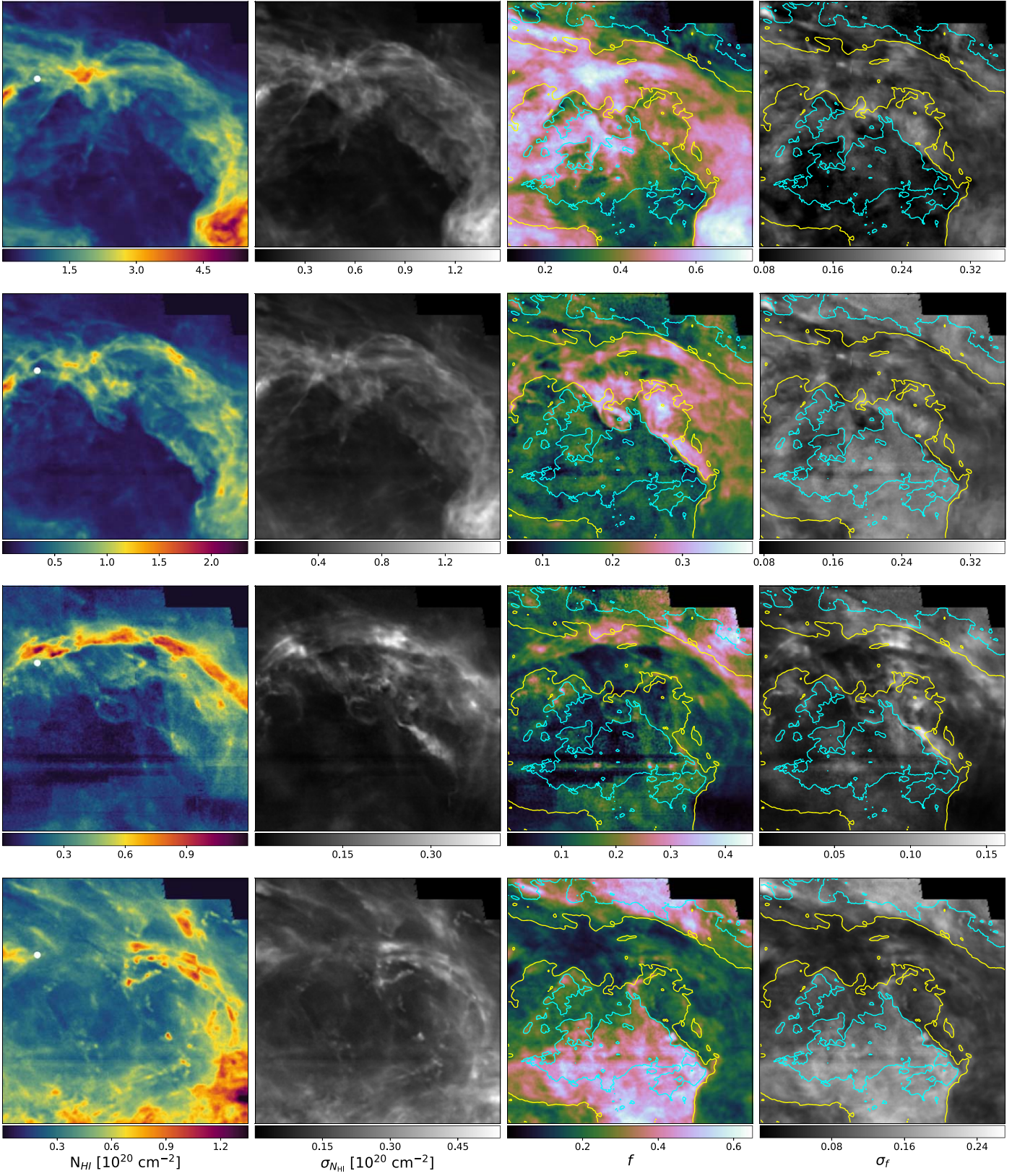


Figure 8. Column density and mass fraction maps (first and third column) with their associated standard deviation maps (second and fourth column) of the thermal phases in the NCPL, obtained using the means and standard deviations of the three methods described in Section 4.2.2. Rows from top to bottom show the CNM, LNM, WNM_A, and WNM_D, respectively. White points in the first column represent the position of the DF absorption source from the DHIGLS survey. Cyan and yellow lines represent contours of the total LVC column density, with levels of 1×10^{20} and $2 \times 10^{20} \text{ cm}^{-2}$, respectively.

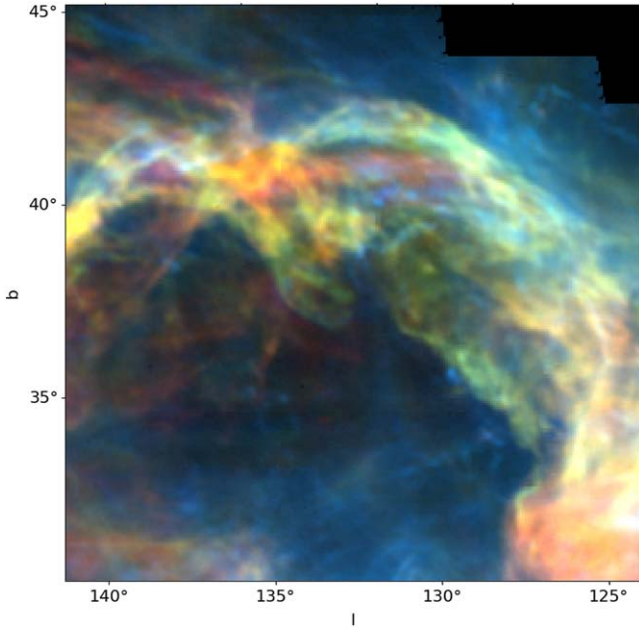


Figure 9. Three-phase view of the NCPL from column density maps of CNM (red), LNM (green), and $\text{WNM}_D + \text{WNM}_A$ (blue). Maps were scaled with natural weightings to highlight their interrelationship and relative column densities.

Table 2

Mean Column Density and Mass Fraction Properties and Their Uncertainties of Phases Inferred from NCPL Data “On Loop” and “Off Loop” Using a Mask with Level $2 \times 10^{20} \text{ cm}^{-2}$ from the Total Column Density of the LVC Model Cube

	$\langle N_{\text{H I}} \rangle$ 10^{20} cm^{-2}	$\langle \sigma_{N_{\text{H I}}} \rangle$ 10^{20} cm^{-2}	$\langle f \rangle$	$\langle \sigma_f \rangle$
On Loop				
CNM	1.71	0.50	0.50	0.15
LNM	0.71	0.50	0.21	0.15
WNM_A	0.12	0.08	0.11	0.04
WNM_D	0.25	0.12	0.16	0.08
Off Loop				
CNM	0.42	0.14	0.36	0.12
LNM	0.19	0.16	0.16	0.14
WNM_A	0.15	0.05	0.13	0.04
WNM_D	0.34	0.16	0.32	0.15

4.4. Anti-correlations between Phases

If the WNM mass fraction is low, as found by Kalberla & Haud (2018) in their Figure 18 right, then the LNM mass fraction and the CNM mass fraction must anti-correlate, by construction (the fractions need to add to 1). In our field covering the NCPL loop and its surroundings, the situation is much more complex, as shown in Figure 10. Both f_{LNM} and f_{WNM_A} are relatively small, and so f_{WNM_D} and f_{CNM} show the most obvious anti-correlation (lower left panel). This can be seen in the morphology of the maps of f_{WNM_D} and f_{CNM} in column 3 of Figure 8, using the column density contours for reference. The upper left endpoint of the anti-correlation corresponds to the lower central area of the map and the area above the loop, where WNM_D dominates, while the lower right endpoint corresponds to the loop, where CNM dominates. Along the loop, in places where there is little WNM, CNM and

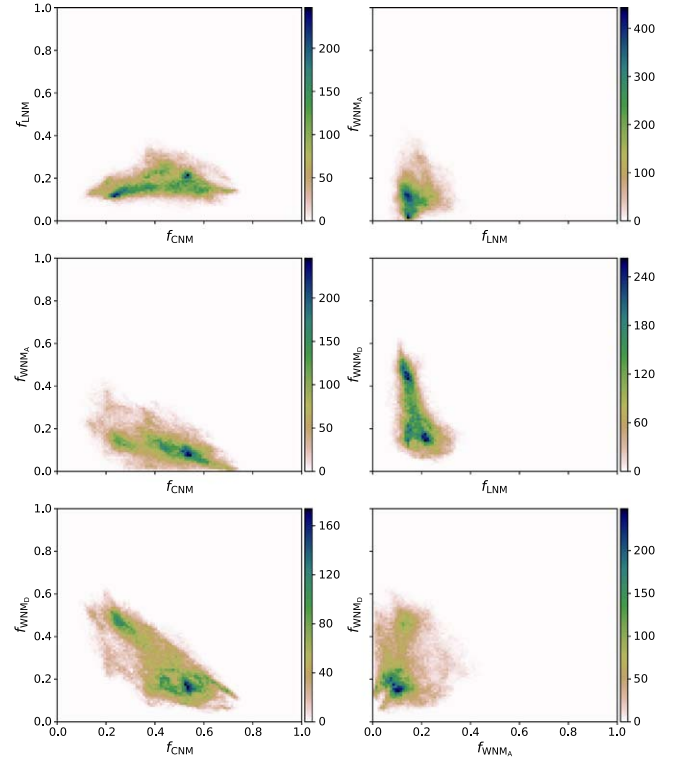


Figure 10. 2D distribution functions, showing how the various phase mass fractions are related to one another. Left column shows the relationship between LNM (top), WNM_A (middle), and WNM_D (bottom) and the CNM. First two rows of the right column show the relationship between the WNM components (WNM_A : top, WNM_D : middle) and the LNM. Bottom right panel shows the relationship between the two WNM components.

LNM can be seen to anti-correlate, and this is reflected in the upper left panel of Figure 10. But elsewhere, there are areas where all phases contribute along the line of sight.

5. Further Evidence of Cold Gas from Absorption Lines in the NCPL

5.1. Absorption Against 4C +71.09

To further investigate the presence of CNM in the NCPL, it is useful to turn to the DF field from the DHIGLS HI survey¹⁰ B17 with the Synthesis Telescope (ST) at the Dominion Radio Astrophysical Observatory. DF is embedded in the NCPL field of GHIGLS and provides a spatial resolution of about $1'$, allowing the detection of radio point sources that have a high continuum brightness temperature, T_c .¹¹ The velocity resolution and channel spacing of the spectrometer were 1.32 km s^{-1} and $\Delta v = 0.824 \text{ km s}^{-1}$, respectively.

5.1.1. Spin Temperature

In their paper, B17 reported the detection of CNM gas in DF against the background radio galaxy 4C+71.09 (NVSS¹² J101132 + 712440, Condon et al. 1998), located within the loop as shown by the white points in Figures 2 and 8. They found a single cold component with spin temperature

¹⁰ DRAO HI Intermediate Galactic Latitude Survey: <https://www.cita.utoronto.ca/DHIGLS/>.

¹¹ T_c depends on the cataloged source flux density and inversely as the square of the beam size; see Equation (8) in B17.

¹² NRAO VLA Sky Survey: <https://www.cv.nrao.edu/nvss/>.

Table 3
Parameters^a of Select Absorption Features, Interpolated Emission, and Derived T_s from DHIGLS and GHIGLS

Region	NVSS Source	T_c	μ_n	σ_n	T_n	μ_b	σ_b	T_b	T_s	σ_{th}	σ_{nt}	f_{CNM}	M_t
DF	J101132+712440	380	5.63	1.30	−75	5.89	1.58	19.11	77	0.80	1.03	0.42	2.6
DF	J101132+712440	380	5.63	1.30	−75	6.00	1.50	15.20	64	0.73	1.08	0.32	3.0
NCPL	J101132+712440	380	5.63	1.30	−75	5.33	2.02	17.56	72.1	0.77	1.05	0.54	2.8
UM	J094912+661459	444	2.43	1.52	−109	2.67	1.77	22.41	76.3	0.80	1.31	0.51	3.3
UM	J094912+661459	444	2.43	1.52	−109	2.66	1.99	22.73	72.2	0.80	1.30	0.55	3.4

Note.

^a Velocities in km s^{-1} and temperatures in K.

$T_s = 84$ K from

$$T_s = T_c T_b / (T_b - T_n), \quad (7)$$

where T_b is the brightness temperature of the cold gas from the emission spectrum interpolated at the position of the source, and T_n is the net temperature of the absorption spectrum. These numbers were taken visually from the original DF data (see Section 8.3 in B17 for further details). In this work, we refine our T_s estimate by modeling the emission-absorption pair with Gaussians to allow for a better estimation of the cold component amplitude.

The absorption spectrum at the position of the source is well described by a single Gaussian component superimposed on a quadratic polynomial to compensate the baseline residual present in the data. Parameters μ_n , σ_n , and T_n of the Gaussian are tabulated in Table 3.

Modeling the emission spectrum requires approximating the total brightness temperature emitted by the gas that would be observed in the absence of the background radio source. This is usually achieved by linear interpolation of the emission spectra in the area surrounding the source (e.g., Heiles & Troland 2003a; Murray et al. 2015, 2018; Syed et al. 2021). Specifically, we calculated the average spectrum taken in an annulus centered on the source with an inner radius $r_{in} = 1/2$ and an outer radius $r_{out} = 3'$ (i.e., 4 and 10 pixels of size $18''$, respectively).

The resulting spectrum is well fitted by a sum of three Gaussians (one for each phase), as shown by the solid lines in Figure 11. Parameters μ_b , σ_b , and T_b of the narrowest Gaussian are tabulated in Table 3 (first row). Using the numbers from Table 3, Equation (7) evaluates to $T_s = 77$ K. This is lower than that found by B17 and is explained by the presence of an intermediate Gaussian, possibly modeling unstable gas, that lowers the amplitude of the cold component. We find a CNM mass fraction, $f_{CNM} = 0.43$ (see Table 3).

Alternatively, we performed a Gaussian fit of a 64×64 pixel grid centered on the source with ROHSA. In that case, three Gaussians are needed to fully encode the signal as well, as shown by the dashed lines in Figure 11). Parameters μ_b , σ_b , and T_b of the narrowest Gaussian at the position of the source are interpolated from the ROHSA parameter maps in the same annulus and are also tabulated in Table 3 (second row). Equation (7) evaluates to $T_s = 64$ K. Here, we find $f_{CNM} = 0.33$ (see Table 3).

In these two alternative decompositions the spectral data being fit on the 64×64 pixels are identical, and so this comparison demonstrates the degeneracy of the solutions that can arise when fitting a nonlinear model like a sum of Gaussians and the sensitivity of the values of derived parameters.

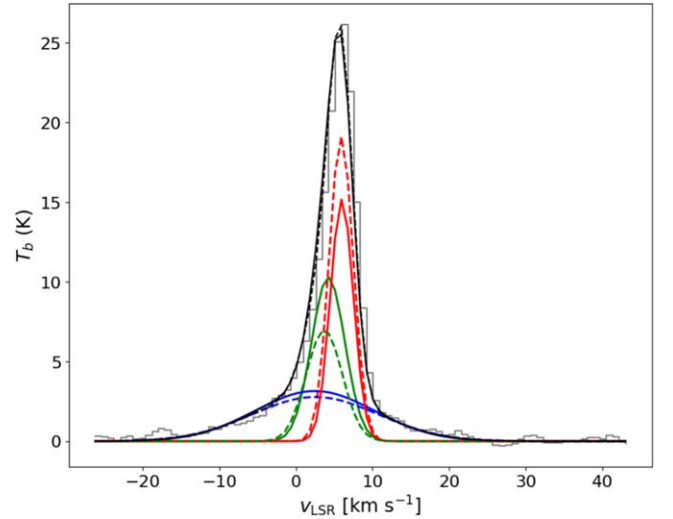


Figure 11. Gaussian decomposition of the averaged emission spectrum taken in a $\sim 2'$ annulus centered on the source. The original signal is shown in gray and the total signal encoded by the Gaussians in black. The three individual Gaussians (solid lines) are color coded by phase, same as Figure 6. Gaussian decomposition by ROHSA from interpolation of the parameter maps in the same annulus is shown with dashed lines and the same color code. Parameters of the narrowest Gaussians are tabulated in Table 3.

5.1.2. Thermal and Nonthermal Broadening

In the CNM, it is believed that collisional excitation alone allows $T_s \simeq T_k$ (Murray et al. 2015), where T_k is the kinetic temperature. It follows that the thermal broadening of the cold component

$$\sigma_{th} = \sqrt{T_k k_B / m_H} \simeq \sqrt{T_s / 121}, \quad (8)$$

where m_H is the mass of hydrogen and k_B is the Boltzmann constant, and the numerical factor is in units of $\text{K km}^{-2} \text{s}^2$. For both of the above methods, Equation (8) evaluates to a smaller dispersion than that of the total broadening of the absorption line, σ_n , which measures the total velocity dispersion of gas along the line of sight, including systematic motions (e.g., velocity gradients), instrumental broadening,¹³ and/or turbulent motions from the energy cascade.

The total broadening of the line is often modeled as a quadrature sum of a thermal component and a nonthermal

¹³ From the channel spacing of the spectrometer, Δv , we found an instrumental line broadening of about 0.36 km s^{-1} , by fitting a Gaussian to a zeroed spectrum, with a single channel set to 1 K.

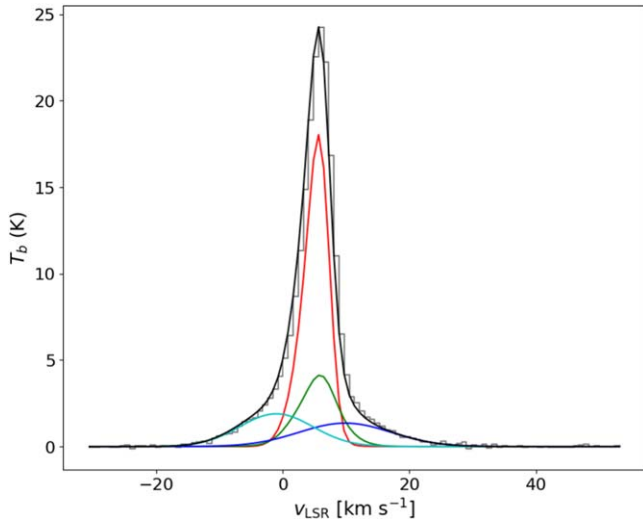


Figure 12. Gaussian decomposition by ROHSA at the absorption position of DF from our final LVC model cube. The original signal is shown in gray and the total brightness temperature encoded by ROHSA is shown in black. Colored lines represent each of the four components, as seen in Figure 8. Red represents CNM, green represents LNM, blue represents WNM_A, and cyan represents WNM_D.

component,

$$\sigma_n^2 = \sigma_{th}^2 + \sigma_{nt}^2, \quad (9)$$

(e.g., Heiles & Troland 2003b; Marchal & Miville-Deschênes 2021; Marchal et al. 2021; Syed et al. 2021). Rearranging Equation (9) to use the entries in the table leads to $\sigma_{nt} \approx 1 \text{ km s}^{-1}$, as entered in Table 3.

The turbulent Mach number is given by

$$M_t^2 = 3\sigma_{nt}^2 / C_{iso}^2 = 4.2\sigma_{nt}^2 / \sigma_{th}^2, \quad (10)$$

where $C_{iso} = \sqrt{\sigma_{th}/\mu}$ is the isothermal sound speed, appropriate in the CNM.¹⁴ Values of M_t are calculated from the dispersions already in the table.

We find $M_t \approx 3$. Although the NCPL is a specific environment, this value is close to the peak of the histogram from all 21-Sponge survey sources analyzed by Murray et al. (2015) (see their Figure 5) and consistent with the earlier findings of Heiles & Troland (2003b), regardless of the environment to which they belong. This could be a coincidence, given that the histograms have a considerable spread.

Comparison of the parameters for absorption and emission reveals that μ_b is shifted by $0.2\text{--}0.3 \text{ km s}^{-1}$ from μ_n , regardless the method used. Similarly, $\sigma_b > \sigma_n$. The simplest explanation is that there is some warmer CNM along the line of sight that is less significant for absorption. If there is gas with somewhat different temperatures, the central velocity might be different too, also increasing σ_b .

5.1.3. Comparison with GHIGLS

Figure 12 shows, at the position of the absorption source, the three-phase (four components) best model obtained with ROHSA from averaging the three series presented in Section 4.2. This spectrum, whose corresponding beam is that of GHIGLS (i.e., $9''.4$), also shows the presence of unstable gas.

¹⁴ The mean molecular weight is μm_H with $\mu = 1.4$. Combined with Equation (9), (10) is equivalent to Equation (17) of Heiles & Troland (2003b).

Note that in this case, the model is constrained by the totality of the PPV cube and not only the emission at the position of the source (or from a small grid around). The resulting CNM component is still well described by a single Gaussian (although it shows a slight asymmetry toward negative velocities). This is compatible with what is seen in absorption. The corresponding Gaussian parameters are tabulated in Table 3 (third row).

As for DHIGLS emission data, the presence of LNM lowers the brightness temperature of the cold gas at $T_b = 17.5 \text{ K}$, yielding a lower spin temperature $T_s = 72 \text{ K}$, and a higher nonthermal broadening of the absorption line. From our best ROHSA model, we find $f_{CNM} = 0.54 \pm 0.1$.

The variations in the physical quantities inferred from the three methods applied to GHIGLS and DHIGLS data reflect the difficulty of modeling the contribution of the CNM from the interpolated spectrum at the position of the absorption source. This translates to an uncertainty of the spin temperature of the gas, the nonthermal contribution to its velocity dispersion, and the CNM mass fraction along the line of sight (of similar amplitude to the uncertainty inferred from the stability analysis shown in Figure 8 (top right panel)).

5.2. Absorption Against 4C +66.09

Although not included in the field analyzed with ROHSA, the DHIGLS survey contains another absorption line located in the NCPL (against Ursa Major), toward the background source 4C +66.09 (NVSS J094912+661459), also shown by a white point in Figure 2. The data from this emission-absorption pair are taken from the UM field, located east of DF. Following the same methodology (i.e., interpolated spectrum and interpolated ROHSA parameters maps), we find that the DHIGLS data are well fitted with two Gaussians (one broad and one narrow). The physical properties of the cold gas are similar to what was found in DF. For completeness, values are tabulated in the last two rows in Table 3.

6. Discussion

6.1. Mass Fraction of CNM

Based on coherent modeling of emission and absorption spectra distributed randomly over the entire intermediate to high-latitude sky (Heiles & Troland 2003a; Murray et al. 2015, 2018; Roy et al. 2013a, 2013b), it has been estimated that about 30% of the H I is in the cold CNM phase, and 20% in the thermally unstable regime. Marchal & Miville-Deschênes (2021) found a similar fraction for the unstable gas in the North Ecliptic Pole (NEP) field of the GHIGLS survey but a much lower fraction of cold gas, about 8%.

By contrast, in the NCPL the mass fraction of CNM is significantly higher, on average 52% in the loop. We take this as an indicator that the dynamical process at the origin of the NCPL has been an effective trigger for the thermal phase transition and formation of the condensed CNM phase.

Similar mass fractions along the part of the loop decomposed with ROHSA (i.e., in Polaris and the Spider) suggest that the gas has been impacted in the much the same way. However, there are significant column density differences along the loop. The Spider is a significant condensation that might reflect a preexisting higher-density region in the ISM being overrun by the dynamical process. In that context, the legs emanating

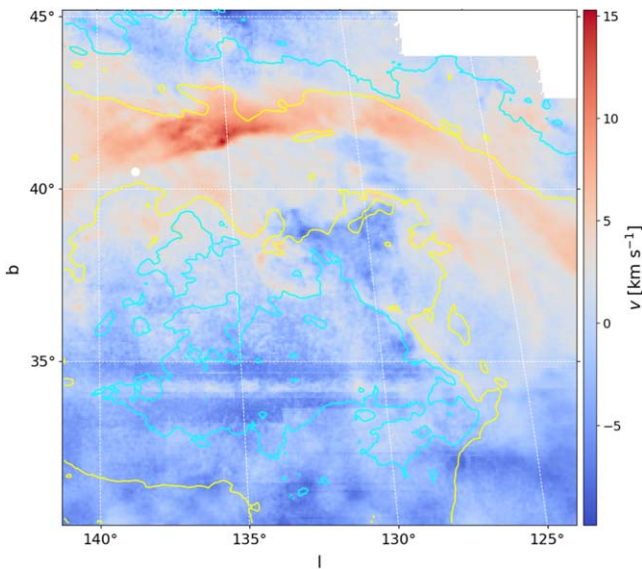


Figure 13. Centroid velocity map of $WNM_A + WNM_D$ from our best model inferred with ROHSA. (The geometric/nonphysical structure in regions of low intensity arises from imperfect stray radiation correction in blocks of the survey observed at different times.) Contours and annotation are the same as in Figure 8.

from the Spider body might also relate to the response to the flow wrapping round this obstacle.

Our best model indicates the presence of unstable gas in the loop, suggesting that the underlying dynamical process giving rise to the LNM phase is still in action. We note that the legs are traced in both high CNM mass fraction and the presence of LNM and that therefore we do not immediately know in which direction the phase transition is occurring.

In the single UM line of sight in Ursa Major, a similarly high CNM mass fraction is observed, about 50%, and the presence of LNM gas remains unclear. The comprehensive mapping of the thermal phases in Ursa Major needed for a comparative study of this part of the loop could be achieved using high-resolution observations from the DHIGLS survey at $1'$.

6.2. Future Work on the Relationship to Other Tracers

On large areas of the high-latitude sky, Clark et al. (2019) and Murray et al. (2020) have shown that the far-IR (FIR) emission from dust grains per H atom probed by Planck increases monotonically with the fraction of cold gas inferred from the GALFA-HI survey (Peek et al. 2011, 2018). However, they could not discriminate between different scenarios that could underlie this effect: the presence of molecular hydrogen yet no CO (CO dark gas), changes in dust emissivity, and/or changes in the dust-to-gas ratio associated with the thermal phase transition.

In principle, our multiphase model offers such an opportunity to reexamine the FIR- N_{HI} correlation in the NCPL. For example, we find high CNM mass fractions in the body of the Spider (about 70%) where the formation of CO was mapped and studied by Barriault et al. (2010). There is excess emission relative to N_{HI} and the dust is cooler (Planck Collaboration XXIV 2011; Planck Collaboration XI 2014). The interrelationships remain to be explored in more detail to understand what conditions can initiate a second phase transition to the molecular phase. In the Spider this would best be done by Gaussian decomposition of the DHIGLS data and Herschel

imaging, both at higher angular resolution than GHIGLS and Planck, respectively.

6.3. Insight into the Origin of the Loop

From our Gaussian decomposition of the NCPL, we have concentrated on the cold/lukewarm gas following the loop. However, the warm gas, combining WNM_D and WNM_A components in a PPV cube, is also of interest. Figure 13 shows the velocity centroid of this gas. There are two features of note: the warm arch tracing the cooler loop as already seen in Figure 8, and the relative motion of the arch, which is related to the velocity gradient noted by Meyerdierks et al. (1991) and motivated their model of an expanding cylinder. In a comprehensive study of a target cloud to the east of the region that we have analyzed, Skolidis et al. (2021) conclude that overall the magnetic field morphology is consistent with an expanding bubble or cylinder.

The remarkable spatial correspondence between this warm moving arch and the cold/lukewarm gas suggests that WNM_A is a relic of the large-scale organized dynamical process that has triggered the phase transition in the loop. The relationship to 3D dust extinction and the topology of extensions of the Local Bubble is discussed in more detail by Marchal & Martin (2022).

7. Summary

Our novel study of the multiphase properties of the North Celestial Pole Loop is based on HI spectra from GHIGLS. We used ROHSA to decompose the spectral data in emission to model their multiphase structure and corroborated this with limited absorption spectra that were available. The main conclusions are as follows.

1. A phase transition took place in the NCPL that led to the formation of a significant fraction of cold gas (about 50% along the loop on average). Similar CNM mass fractions are observed in Polaris, the Spider and Ursa Major, suggesting a common origin of the dynamical process that triggered the thermal condensation. Our best model contains the presence of unstable gas, which suggests that the dynamical process at the origin of this condensation is still in action.
2. From absorption line measurement, we find that turbulence in the cold phase is similar in the Spider and Ursa Major and is supersonic with a turbulent sonic Mach number of about 3. This value is close to the peak of the histogram ($M_t \sim 3$) of all 21-Sponge survey sources analyzed by Murray et al. (2015).
3. We observe the presence of a well-defined warm arch associated with the loop, whose projected component of the velocity field is about 14 km s^{-1} . The spatial correlation between this arch and the cold/lukewarm part of the loop suggests that it could be a relic of the large-scale organized dynamical process that triggered the phase transition.

Extending the scope of this study are many possible future investigations. For example, Zeeman measurements of the magnetic field strength by Heiles (1989) could be correlated with the CNM mass fraction to investigate the influence of the magnetic field on dynamics and phase transitions, as can also be explored in numerical simulations such as by Valdivia et al. (2016). Another possibility would be to study the physical

properties of the H I structures found by segmentation of CNM, LNM, and WNM maps (Marchal et al. 2021). This might best be done starting with a ROHSA decomposition of the higher-resolution DF data.

We acknowledge support from the Natural Sciences and Engineering Research Council (NSERC) of Canada. This work took place under the Summer Undergraduate Research Program (SURP), hosted by the University of Toronto. This research has also made use of the NASA Astrophysics Data System. We appreciate enlightening conversations with M.-A. Miville-Deschênes and F. Buckland-Willis. We thank the anonymous referee whose comments and suggestions have improved this manuscript.

Software: AstroPy, a community-developed core Python package for Astronomy (Astropy Collaboration et al. 2013, 2018), CMasher van der Velden (2020), NumPy (van der Walt et al. 2011), Matplotlib (Hunter 2007), and, scikit-image (van der Walt 2014), and SciPy (Virtanen et al. 2020).

Appendix A In-painting

In directions where there is identifiable extra-Galactic emission within the spectral range being analyzed (including emission-free end channels), the ROHSA decomposition modeling the Galactic emission can be affected, either “wasting” Gaussians to fit this contaminating emission, or leaving large residuals.

A main area of contamination is the large polygon seen in the left panel of Figure A1. For the modeling here of LVC or IVC emission, this polygon was defined conservatively to contain the emission of M81 (Adler & Westpfahl 1996) and other members of the group, including M82, NGC 3077, and NGC 2976 near the west, north, and east apices, respectively, and the widespread tidally disturbed gas (Yun et al. 1994, 2000; Chynoweth et al. 2008; de Blok et al. 2018; Sorgho et al. 2019).

(This polygon also includes the GHIGLS-supplied mask of positions at which it was not possible to remove spectral baselines.) In cropping the region to be analyzed here, we

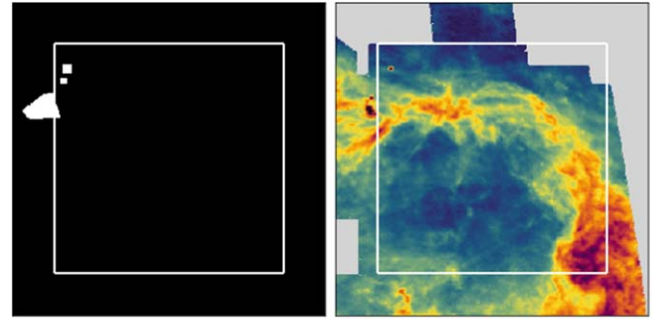


Figure A1. Polygons (white regions in left panel) were developed to isolate contaminating extra-Galactic emission. This contamination can be seen in the map of the total column density (right) and is removed channel by channel by in-painting, with the final result seen in Figure 2. The large white box outlines the subregion of the data that we chose to focus on for the analysis.

deliberately avoided most of this polygon, but it is unavoidable in the field studied by L. Vujeva et al. (2022, in preparation) toward Ursa Major to the east.

The two smaller polygons to the north contain emission near HIJASS J1029+68 and IC 2574, respectively (Chynoweth et al. 2009; Sorgho et al. 2019).

These polygons were then in-painted channel by channel using a built-in tool from SciPy: `scipy.interpolate.griddata()`, adopting simple linear interpolation in spanning these sizable polygons. After the ROHSA decomposition, these polygons are masked in further quantitative analysis.

Appendix B Maps of Individual Gaussian Components

Figure B1 shows the column density maps of each Gaussian sorted by increasing column-density-weighted mean velocities (see Table 2). Figures B2 and B3 show the corresponding velocity fields and dispersion velocity fields. Note, the labels overlaid on the panels in Figure B1 help to associate them with the clusters in Figure 5: e.g., for G_7 (row 2, column 1), “LVC/CNM 1.72” indicates the velocity range, the thermal phase, and the column-density-weighted mean velocity dispersion $\langle\sigma_n\rangle$ in km s^{-1} as tabulated in Table 1.

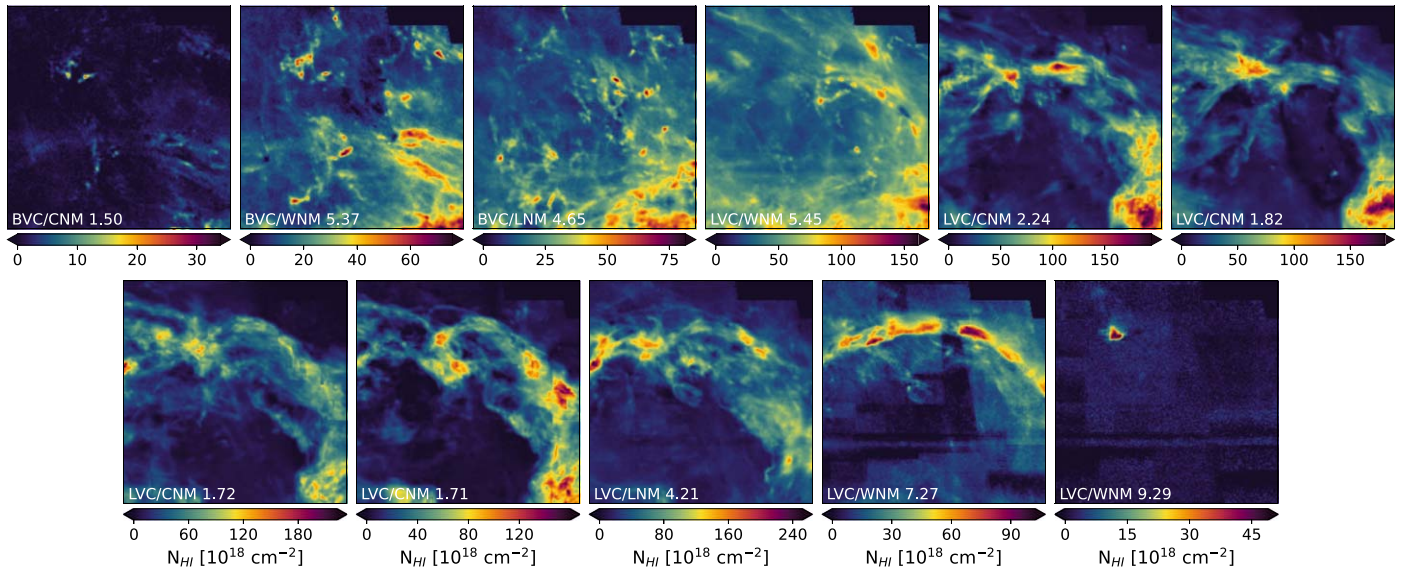


Figure B1. Mosaic of N_{HI} maps of the individual Gaussian components. The maps are sorted by mean velocity. The labels in the bottom left corner represent the sorting of that particular Gaussian component. The number beside this label is the mean velocity dispersion (σ) in units of km s^{-1} . Note the different ranges of the color bars.

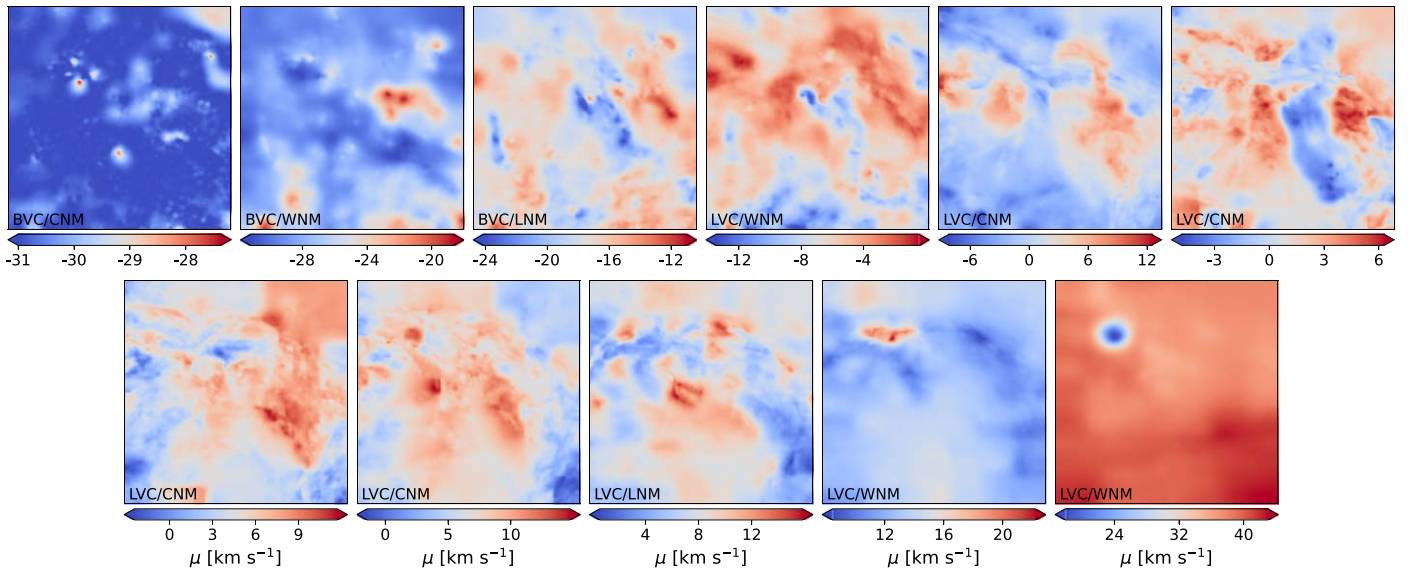


Figure B2. Mosaic like Figure B1, but of maps of the mean velocity, μ , of the individual Gaussian components.

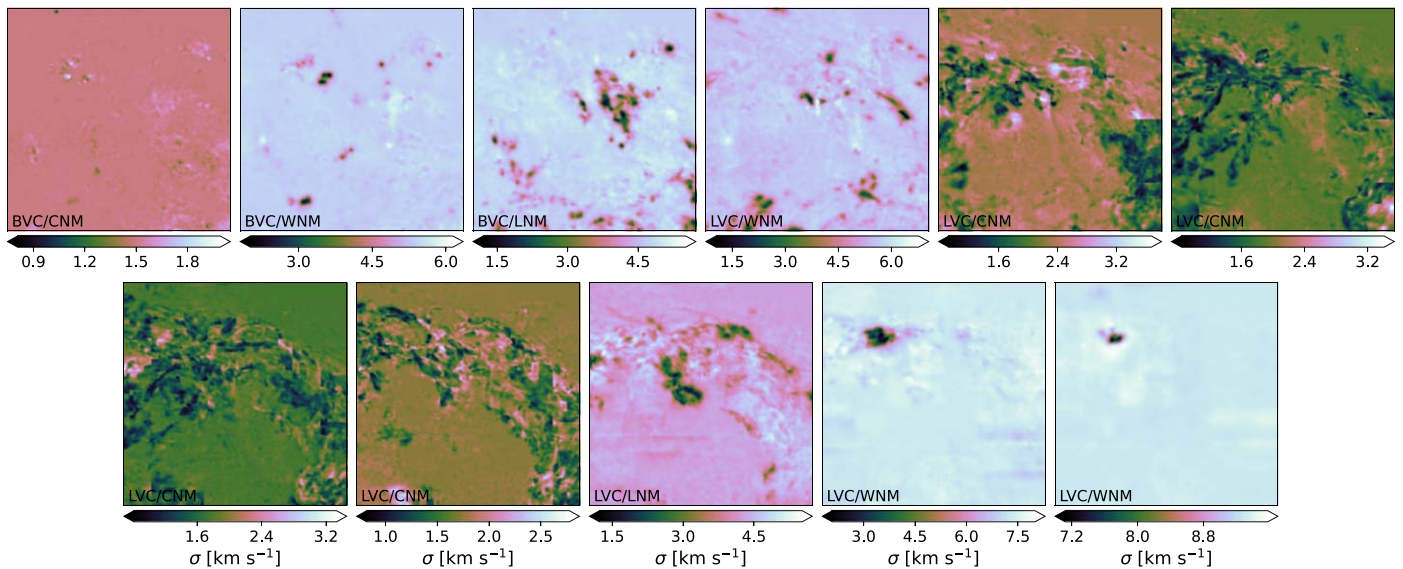


Figure B3. Mosaic like Figure B1, but of maps of the velocity dispersion, σ , of the individual Gaussian components.

ORCID iDs

Mukesh Taank <https://orcid.org/0000-0001-8461-5552>
 Antoine Marchal <https://orcid.org/0000-0002-5501-232X>
 Peter G. Martin <https://orcid.org/0000-0002-5236-3896>
 Luka Vujeva <https://orcid.org/0000-0001-7697-8361>

References

- Adler, D. S., & Westpfahl, D. J. 1996, *AJ*, **111**, 735
 Astropy Collaboration, Price-Whelan, A. M., Sipőcz, B. M., et al. 2018, *AJ*, **156**, 123
 Astropy Collaboration, Robitaille, T. P., Tollerud, E. J., et al. 2013, *A&A*, **558**, A33
 Barriault, L., Joncas, G., Falgarone, E., et al. 2010, *MNRAS*, **406**, 2713
 Bellomi, E., Godard, B., Hennebelle, P., et al. 2020, *A&A*, **643**, A36
 Blagrove, K., Martin, P. G., Joncas, G., et al. 2017, *ApJ*, **834**, 126
 Boothroyd, A. I., Blagrove, K., Lockman, F. J., et al. 2011, *A&A*, **536**, A81
 Chynoweth, K. M., Langston, G. I., Holley-Bockelmann, K., & Lockman, F. J. 2009, *AJ*, **138**, 287
 Chynoweth, K. M., Langston, G. I., Yun, M. S., et al. 2008, *AJ*, **135**, 1983
 Clark, S. E., Peek, J. E. G., & Miville-Deschênes, M. A. 2019, *ApJ*, **874**, 171
 Condon, J. J., Cotton, W. D., Greisen, E. W., et al. 1998, *AJ*, **115**, 1693
 de Blok, W. J. G., Walter, F., Ferguson, A. M. N., et al. 2018, *ApJ*, **865**, 26
 Field, G. B. 1965, *ApJ*, **142**, 531
 Field, G. B., Goldsmith, D. W., & Habing, H. J. 1969, *ApJL*, **155**, L149
 Heiles, C. 1984, *ApJS*, **55**, 585
 Heiles, C. 1989, *ApJ*, **336**, 808
 Heiles, C., & Troland, T. H. 2003a, *ApJS*, **145**, 329
 Heiles, C., & Troland, T. H. 2003b, *ApJ*, **586**, 1067
 Hennebelle, P., & Pérault, M. 1999, *A&A*, **351**, 309
 Hunter, J. D. 2007, *CSE*, **9**, 90
 Kalberla, P., & Haud, U. 2018, *A&A*, **619**, A58
 Kerp, J., Winkel, B., Ben Bekhti, N., Flöer, L., & Kalberla, P. M. W. 2011, *AN*, **332**, 637
 Marchal, A., & Martin, P. G. 2022, *ApJ*, submitted
 Marchal, A., Martin, P. G., & Gong, M. 2021, *ApJ*, **921**, 11
 Marchal, A., & Miville-Deschênes, M.-A. 2021, *ApJ*, **908**, 186
 Marchal, A., Miville-Deschênes, M.-A., Orieux, F., et al. 2019, *A&A*, **626**, A101
 Martin, P. G., Blagrove, K. P. M., Lockman, F. J., et al. 2015, *ApJ*, **809**, 153
 Meyerderks, H., Heithausen, A., & Reif, K. 1991, *A&A*, **245**, 247
 Murray, C. E., Peek, J. E. G., & Kim, C.-G. 2020, *ApJ*, **899**, 15
 Murray, C. E., Stanimirović, S., Goss, W. M., et al. 2018, *ApJS*, **238**, 14
 Murray, C. E., Stanimirović, S., Goss, W. M., et al. 2015, *ApJ*, **804**, 89
 Peek, J. E. G., Babler, B. L., Zheng, Y., et al. 2018, *ApJS*, **234**, 2
 Peek, J. E. G., Heiles, C., Douglas, K. A., et al. 2011, *ApJS*, **194**, 20
 Planck Collaboration XXIV 2011, *A&A*, **536**, A24
 Planck Collaboration XI 2014, *A&A*, **571**, A11
 Roy, N., Kanekar, N., Braun, R., & Chengalur, J. N. 2013a, *MNRAS*, **436**, 2352
 Roy, N., Kanekar, N., & Chengalur, J. N. 2013b, *MNRAS*, **436**, 2366
 Rybarczyk, D. R., Stanimirović, S., Gong, M., et al. 2022, *ApJ*, **928**, 79
 Saury, E., Miville-Deschênes, M. A., Hennebelle, P., Audit, E., & Schmidt, W. 2014, *A&A*, **567**, A16
 Seifried, D., Schmidt, W., & Niemeyer, J. C. 2011, *A&A*, **526**, A14
 Skolidis, R., Tassis, K., Panopoulou, G., et al. 2021, arXiv:2110.11878
 Sorgho, A., Foster, T., Carignan, C., & Chemin, L. 2019, *MNRAS*, **486**, 504
 Syed, J., Soler, J. D., Beuther, H., et al. 2021, *A&A*, **657**, A1
 Valdivia, V., Hennebelle, P., Gérin, M., & Lesaffre, P. 2016, *A&A*, **587**, A76
 van der Velden, E. 2020, *JOSS*, **5**, 2004
 van der Walt, S., Colbert, S. C., & Varoquaux, G. 2011, *CSE*, **13**, 22
 van der Walt, S., Schönberger, J. L., Nunez-Iglesias, J., et al. 2014, *PeerJ*, **2**, e453
 Virtanen, P., Gommers, R., Oliphant, T. E., et al. 2020, *NatMe*, **17**, 261
 Winkel, B., Kerp, J., Flöer, L., et al. 2016, *A&A*, **585**, A41
 Yun, M. S., Ho, P. T. P., & Lo, K. Y. 1994, *Natur*, **372**, 530
 Yun, M. S., Ho, P. T. P., & Lo, K. Y. 2000, in ASP Conf. Ser. 217, Imaging at Radio through Submillimeter Wavelengths, ed. J. G. Mangum & S. J. E. Radford (San Francisco, CA: ASP), 374